Smooth Functional and Structural Maps on the Neocortex Via Orthonormal Bases of the Laplace–Beltrami Operator

Anqi Qiu*, Dmitri Bitouk, and Michael I. Miller, *Senior Member, IEEE*

***Abstract*—Functional and structural maps, such as a curvature, cortical thickness, and functional magnetic resonance imaging (MRI) maps, indexed over the local coordinates of the cortical manifold play an important role in neuropsychiatric studies. Due to the highly convoluted nature of the cerebral cortex and image quality, these functions are generally uninterpretable without proper methods of association and smoothness onto the local coordinate system. In this paper, we generalized the spline smoothing problem (Wahba, 1990) from a sphere to any arbitrary two-dimensional (2-D) manifold with boundaries. We first seek a numerical solution to orthonormal basis functions of the Laplace–Beltrami (LB) operator with Neumann boundary conditions for a 2-D manifold $\mathcal{M}$ then solve the spline smoothing problem in a reproducing kernel Hilbert space (r.k.h.s.) of real-valued functions on manifold $\mathcal{M}$ with kernel constructed from the basis functions. The explicit discrete LB representation is derived using the finite element method calculated directly on the manifold coordinates so that finding discrete LB orthonormal basis functions is equivalent to solving an algebraic eigenvalue problem. And then smoothed functions in r.k.h.s can be represented as a linear combination of the basis functions. We demonstrate numerical solutions of spherical harmonics on a unit sphere and brain orthonormal basis functions on a planum temporale manifold. Then synthetic data is used to quantify the goodness of the smoothness compared with the ground truth and discuss how many basis functions should be incorporated in the smoothing. We present applications of our approach to smoothing sulcal mean curvature, cortical thickness, and functional statistical maps on submanifolds of the neocortex.**

***Index Terms*—Cortical thickness, curvature, Laplace–Beltrami (LB) operator, Neumann boundary conditions, reproducing kernel Hilbert space, spline smoothing.**

I. Introduction

THE human cerebral cortex can be modeled as a highly convoluted sheet. Its shape and local structure are studied and play an important role in understanding neurodegenerative and psychiatric disorders. Therefore, quantitative functions, such as cortical thickness, curvature, and functional statistical maps indexed over the brain manifold, provide tools for understanding anatomical structures and functions of normal brain as well as brain affected by neurodegenerative diseases (e.g., [1] and [2]). Due to the low resolution of magnetic resonance (MR) images and errors in extraction of brain manifolds, smoothing functions on the brain manifold is needed to increase signal-to-noise ratio [3] as well as the power of statistical analysis on these cortical functions (e.g., [4] and [5]).

A well-known approach to smooth data is the diffusion smoothing approach based on the Laplace operator that has been widely used in removing noise on regular grid images (e.g., [6]). However, the Laplace operator has been applied to smoothing functions on brain manifolds in a small number of groups [4], [5], [7]–[14]. Another way to smooth functions on manifolds is the spline interpolation using manifold's basis functions, which received great attention for a sphere case [15]. This idea of smoothing or regularizing data on an arbitrary two-dimensional (2-D) manifold has not been investigated possibly due to the fact that there are no closed form expressions of orthonormal basis functions available for the manifold.

This paper generalizes the spline interpolation approach from a sphere to a 2-D manifold by seeking numerical solutions to orthonormal basis functions for the 2-D manifold. The intuition behind is that a complete set of real-valued orthonormal basis functions on a Riemannian manifold will be serve as the substitution to Fourier basis functions on the regular grid image. From the stochastic signal processing point of view, the procedure of filtering functions on the manifold is simply equivalent to estimating coefficients associated with orthonormal basis functions selected by the filter. We consider the data model

$$y_i = f(x_i) + \epsilon_i, \quad i = 1, 2, \cdots, N$$

where ϵ_i are independent and identically distributed (i.i.d.) Gaussian distributed with mean zero and standard deviation σ. The following spline smoothing problem:

$$\min_{f \in C^2(\mathcal{M})} \gamma \int_{\mathcal{M}} \|\nabla f\|^2 d\mathcal{M} + \sum_{i=1}^{n} (y_i - f(x_i))^2$$

can be solved for a 2-D Riemannian manifold $\mathcal{M}$. The solution is found in a reproducing kernel Hilbert space (r.k.h.s.) of real-valued functions in $C^2(\mathcal{M})$ constructed by orthonormal basis functions. Such basis functions can be found using the

Manuscript received October 18, 2005; revised July 20, 2006. This work was supported by the National Institutes of Health under Grant 1 P41 15241-01A1, Grant 1 R01 EB00975, and Grant 1 P20 MH621130-01A1. *Asterisk indicates corresponding author.*

*A. Qiu is with the Department of Electrical and Computer Engineering and the Center for Imaging Science, The Johns Hopkins University, Baltimore, MD 21218 USA (e-mail: anqi@cis.jhu.edu).

D. Bitouk is with the Department of Electrical and Computer Engineering and the Center for Imaging Science, The Johns Hopkins University, Baltimore, MD 21218 USA.

M. I. Miller is with the Center for Imaging Science and the Department of Biomedical Engineering, The Johns Hopkins University, Baltimore, MD 21218 USA.

Digital Object Identifier 10.1109/TMI.2006.882143

Laplace–Beltrami (LB) operator that is a generalization of the Euclidean representation of the Laplace operator to an arbitrary Riemannian manifold. Due to the LB self-adjoint property, its eigenfuctions form a complete set of real-valued orthonormal basis functions [16]. In general, there are no closed form expressions for the LB basis functions on a curved manifold. We explicitly generate the orthonormal basis functions for each cortical manifold with boundaries using the finite element method (FEM) [17], [18] and show seeking the basis functions is equivalent to solving an algebraic eigenvalue problem.

The remainder of this paper is organized as follows. Section II reviews the spline smoothing problem and its solution represented by analytic spherical harmonics on a unit sphere, which will be generalized to an arbitrary 2-D manifold in Section IV. We start with a variational problem for finding the complete set of LB orthonormal basis functions in Section III-B. Then we present numerical implementation for computing LB orthonormal basis functions by FEM in Section III-C and illustrate numerical solutions to the orthonormal basis functions on a unit sphere and a brain manifold in Section III-D. The smoothing problem is considered in Section IV. In Section V, we quantify mean square error (MSE) of smoothed functions compared to ground truth using synthetic data and present applications of our approach to smoothing mean curvature, cortical thickness, and functional statistical maps on the brain submanifolds: cingulate, planum temporale, and occipital lobe.

II. Previous Work—Spline Smoothing on a Unit Sphere

Assume S is a unit sphere defined on the polar coordinates (θ, ϕ) and p_i is a point on S. The LB orthonormal basis functions on the sphere are referred as spherical harmonics Y_{ls}, $s = -l, \ldots, l$, $l = 0, 1, \ldots$, where

$$\begin{aligned} Y_{ls}(\theta,\phi) &= \theta_{ls}\cos(s\theta)P_l^s(\sin(\phi)), \quad 0 < s \le l, \quad l = 0, 1, \cdots \\ &= \theta_{ls}\sin(s\theta)P_l^{|s|}(\sin(\phi)), \quad -l \le s < 0 \\ &= \theta_{l0}P_l(\sin(\phi)) \quad , s = 0 \end{aligned} \tag{1}$$

where

$$\begin{aligned} \theta_{ls} &= \sqrt{2}\sqrt{\frac{2l+1}{4\pi}\frac{(l-|s|)!}{(l+|s|)!}}, \quad s \neq 0 \\ &= \sqrt{\frac{2l+1}{4\pi}}, \quad s = 0. \end{aligned}$$

P_l^s are the Legendre functions and P_l are the Legendre polynomials. The eigenvalues are $l(l+1)$ associated with Y_{ls}.

Assume $\epsilon = (\epsilon_1, \epsilon_2, \ldots,)^t \sim \mathcal{N}(0, \sigma^2 I)$. Given noisy data from the model

$$y_i = f(p_i) + \epsilon_i, \quad i = 1, 2, \ldots, n \tag{2}$$

the smooth representation of f can be obtained by minimizing

$$\hat{f}(\cdot) = \underset{f(\cdot)\in C^2(S)}{\arg\min}\ \gamma \int_S \|\nabla f\|^2 dS + \sum_{i=1}^{N} \left(y_i - f(p_i)\right)^2. \tag{3}$$

This expression includes the residual sum of squares and "smoothness" of the solution, as represented by the square integral of the first derivative. γ penalizes the smoothness and fidelity to the data. Since the LB eigenfunctions form a complete set of orthonormal basis functions, the solution to the above problem in (3) can be written over the basis Y_{ls} with coefficient κ_{ls} as

$$f = f_{00} + \sum_{l=1}^{n}\sum_{s=-l}^{l} \kappa_{ls} Y_{ls}. \tag{4}$$

As a consequence, solving the smoothing problem in (3) is equivalent to estimating κ_{ls} as

$$\begin{aligned} \hat{\kappa}_{ls} = \underset{\kappa_{ls}}{\arg\min}\, \gamma \sum_{l=1}^{n}\sum_{s=-l}^{l} l(l+1)\kappa_{ls}^2 \\ + \sum_{i=1}^{N}\left(y_i - \sum_{l=0}^{n}\sum_{s=-l}^{l}\kappa_{ls}Y_{ls}(p_i)\right)^2. \end{aligned} \tag{5}$$

Arranging the index set (l, s) in a convenient order, and letting $\boldsymbol{\kappa}$ and $\mathbf{y}$ be vectors of κ_{ls} and y_i and X be the matrix with i, lsth entry $Y_{ls}(p_i)$, we have that (5) in matrix form is

$$\gamma \boldsymbol{\kappa}^t D^{-1} \boldsymbol{\kappa} + \|\boldsymbol{\kappa} - X\boldsymbol{\kappa}\|^2 \tag{6}$$

where D is the diagonal matrix with ls, lsth entry $1/l(l+1)$. When $l = 0$, the corresponding entry of D is zero. ^{t} denotes transpose. The minimizing vector $\boldsymbol{\kappa}$ is

$$\boldsymbol{\kappa} = (X^t X + \gamma D^{-1})^{-1} X^t \mathbf{y}. \tag{7}$$

Although splines on the unit sphere have received great attention [15], the idea of data smoothing or regularization as shown above has not been investigated for any arbitrary 2-D manifold, partly due to the fact that there are no analytic solutions to basis functions for it. In the following, we generalize the above smoothing procedure to arbitrary manifolds by first computing numerical solutions to LB orthonormal basis functions and then solving the spline smoothing problem in (3).

III. Spectral Analysis of the LB Operator

A. Preliminaries

We briefly review some fundamental concepts from differential geometry that are necessary to develop the framework for data smoothing and interpolation on 2-D manifolds. Consider a smooth orientable manifold $\mathcal{M}$ embedded into $\mathbb{R}^3$. We choose to describe $\mathcal{M}$ by means of a parametrization $\mathbf{x} : \mathcal{D} \subset \mathbb{R}^2 \mapsto \mathbb{R}^3$

$$\mathbf{x}(\mathbf{u}) = \begin{bmatrix} x_1(\mathbf{u}) \\ x_2(\mathbf{u}) \\ x_3(\mathbf{u}) \end{bmatrix} \tag{8}$$

where $\mathbf{u} = (u_1, u_2) \in \mathcal{D}$. The parameters u_1 and u_2 play the role of local coordinates on the manifold. It should be noted that there are many ways to construct manifold parametrization and select local coordinates. However, our results in the subsequent sections will be independent of any manifold parametrization.

In this paper, we assume that the map $\mathbf{x}:\mathcal{D}\subset\mathbb{R}^2\mapsto\mathbb{R}^3$ is twice continuously differentiable. At any point $\mathbf{x}(\mathbf{u})\in\mathcal{M}$ on the manifold, the vectors $\partial\mathbf{x}/\partial u_1$ and $\partial\mathbf{x}/\partial u_2$ span the tangent space $\mathcal{T}_{\mathbf{x}(\mathbf{u})}(\mathcal{M})$. The metric properties of the manifold $\mathcal{M}$ can be easily deduced by considering two infinitely close points on the manifold with coordinates $\mathbf{u}$ and $\mathbf{u}+d\mathbf{u}$. Then, the distance ds between them is determined by

$$ds^2=\langle d\mathbf{x},d\mathbf{x}\rangle=\sum_{\alpha,\beta}g_{\alpha\beta}du_\alpha du_\beta \tag{9}$$

where $g_{\alpha\beta}=\langle(\partial\mathbf{x}/\partial u_\alpha),(\partial\mathbf{x}/\partial u_\beta)\rangle$ and the bilinear form in (9) is called the first fundamental form of $\mathcal{M}$. The squared root of the determinant of g is equal to the area of the parallelogram formed by the vectors $(\partial\mathbf{x}/\partial u_1)$ and $(\partial\mathbf{x}/\partial u_2)$

$$\sqrt{\det g}=\sqrt{g_{11}g_{22}-g_{12}^2}=\left\|\frac{\partial\mathbf{x}}{\partial u_1}\times\frac{\partial\mathbf{x}}{\partial u_2}\right\|. \tag{10}$$

Introducing the area element $d\mathcal{M}=\sqrt{\det g(\mathbf{u})}$, one may write down the area $|\mathcal{M}|$ as [19]

$$|\mathcal{M}|=\int_{\mathcal{M}}d\mathcal{M}=\int_{\mathcal{D}}\sqrt{\det g(\mathbf{u})}d\mathbf{u}. \tag{11}$$

Furthermore, we will use the following shorthand notation for the manifold integrals:

$$\int_{\mathcal{M}}f(\mathbf{u})d\mathcal{M}=\int_{\mathcal{D}}f(\mathbf{u})\sqrt{\det g(\mathbf{u})}d\mathbf{u}. \tag{12}$$

Given a smoothly differentiable function $f:\mathcal{D}\mapsto\mathbb{R}$, the intrinsic gradient of f with respect to the parametrization $\mathbf{x}(\mathbf{u})$ is defined as [20]

$$\nabla_{\mathcal{M}}f=\sum_{\alpha,\beta}g^{\alpha\beta}\frac{\partial f}{\partial u_\beta}\frac{\partial\mathbf{x}}{\partial u_\alpha} \tag{13}$$

where $\begin{bmatrix}g^{11}&g^{12}\\g^{21}&g^{22}\end{bmatrix}=g^{-1}$. The LB operator is a generalization of the Euclidean Laplacian to arbitrary differentiable manifolds and is defined as the divergence of the gradient $\triangle_{\mathcal{M}}=\nabla_{\mathcal{M}}\cdot\nabla_{\mathcal{M}}$. For any twice differentiable function $f\in C^2(\mathcal{M})$, the LB operator can be expressed in the following form:

$$\triangle_{\mathcal{M}}f=\frac{1}{\sqrt{g}}\sum_{\alpha,\beta}\frac{\partial}{\partial u_\alpha}\left(\sqrt{g}g^{\alpha\beta}\frac{\partial f}{\partial u_\beta}\right). \tag{14}$$

B. Orthonormal Basis of the LB Operator With Neumann Boundary Conditions

The LB operator is self-adjoint with respect to the $\mathcal{L}_2$ norm defined on the space of continuous piecewise linear functions [21]. We seek eigenvalues and orthonormal basis functions of the LB operator with Neumann boundary conditions on a Riemannian manifold $\mathcal{M}$ embedded into $\mathbb{R}^3$. The Neumann boundary conditions are required to satisfy the condition that any function defined on $\mathcal{M}$ is continuous across the boundary of $\mathcal{M}$, $\partial\mathcal{M}$. The LB eigenvalue problem is posed as

$$\Delta\phi(\mathbf{u})+\lambda\phi(\mathbf{u})=0\text{ in }\mathcal{M} \tag{15}$$

$$\int_{\mathcal{M}}|\phi(\mathbf{u})|^2\,d\mathcal{M}=1 \tag{16}$$

$$\langle\nabla\phi(\mathbf{u}),\mathbf{n}\rangle|_{\partial\mathcal{M}}=0 \tag{17}$$

where Δ is the LB operator; $\mathbf{n}$ is the normal vector on $\partial\mathcal{M}$. LB eigen-elements are denoted as $(\phi(\mathbf{u}),\lambda)$. Equations (15)–(17) are, respectively, partial differential equation of the LB eigenvalue problem, normalization equation to guarantee that the norm of an eigenfunction with respect to manifold $\mathcal{M}$ is one, and equation for Neumann boundary conditions.

The weak form of the LB eigenvalue problem [22] is written as follows. The variational principle for λ takes the form

$$[\lambda]=E(\psi(\cdot))\text{ or }\lambda=S.V.\{E(\phi(\cdot))\} \tag{18}$$

where

$$E(\phi(\cdot))=\frac{\int_{\mathcal{M}}\|\nabla\phi(\mathbf{u})\|^2\,d\mathcal{M}}{\int_{\mathcal{M}}|\phi(\mathbf{u})|^2\,d\mathcal{M}}. \tag{19}$$

$\phi(\mathbf{u})$ are critical points of E in $C^2(\mathcal{M})$ when $\int_{\mathcal{M}}|\phi(\mathbf{u})|^2d\mathcal{M}>0$ and $\phi(\mathbf{u})$ are subject to the boundary conditions in (17). The sign [ ] takes account of the approximate nature of λ when ϕ is not the exact function, and the symbol $S.V.$ means "the stationary value of" (see proof in the Appendix).

Analytic solutions to the LB orthonormal basis functions and eigenvalues cannot always be found for an arbitrary manifold. We will seek the numerical solution to orthonormal basis functions by finding the critical points of E using FEM in the subsequent section.

C. Solving the Eigenvalue Problem via FEM

Now we describe the implementation of the FEM for finding the LB orthonormal basis step by step. Before generating the complete orthonormal basis (CON) functions on the cortex, we have to construct the triangulated mesh for each volume. This consists of three steps: 1) segmentation of the MR tissue as white matter, gray matter, and cerebrospinal fluid (CSF) voxels using Bayesian segmentation [23], [24]; 2) three-dimensional (3-D) isocontouring [24]; based on the intensity value at which there is equal probability of the gray and white matter via matching tetrahedral algorithm; 3) dynamic programming delineation of the boundary of the associated gyral and sulcal submanifolds, from which the submanifold of interest is automatically extracted from the manifold masked by subvolume region-of-interest (ROI) [25], [26].

1) FEM for Generation of the CON:

Construct Triangulated Mesh of Vertices: Define a triangle T_i with area A_i, with vertex locations $\mathbf{u}_{i_1}$, $\mathbf{u}_{i_2}$, and $\mathbf{u}_{i_3}$. Let N_T be the number of triangles on the triangulated mesh, and N_v be

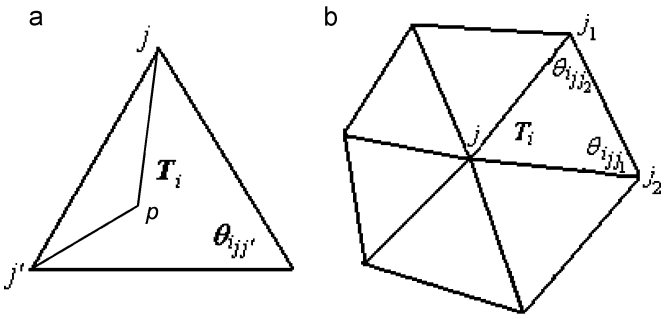

Fig. 1. (a) Illustrates one single triangle T_i with edge jj' and its opposite angle $\theta_{i_{jj'}}$. p is a point inside the triangle. (b) Shows one ring centered at vertex j. Triangle T_i has three vertices: j; j_1; and j_2. $\theta_{i_{jj_1}}$ and $\theta_{i_{jj_2}}$ are angles opposite to edges jj_1 and jj_2, respectively.

the number of vertices. Define $N_T(j)$ as the set of triangles containing vertex j, and $N_T(i,j)$ as the set of triangles containing edge (i,j). $\theta_{i_{jj'}}$ denotes the angle opposite to the edge jj' in triangle T_i [shown Fig. 1(a)]. Let the indices of the three vertices in the triangle T_i be j, j_1, and j_2, respectively.

Construct Discrete Version of E: Let $\phi_{T_i}(\mathbf{u})$ be a linear approximation of $\phi(\mathbf{u})$ within T_i in the barycentric coordinate representation [17], [18], $\phi_{T_i}(\mathbf{u}) = \alpha_{i_1}(\mathbf{u})\phi(\mathbf{u}_{i_1}) + \alpha_{i_2}(\mathbf{u})\phi(\mathbf{u}_{i_2}) + \alpha_{i_3}(\mathbf{u})\phi(\mathbf{u}_{i_3})$, $\sum_{j=1}^{3}\alpha_{i_j}(\mathbf{u}) = 1, 0 \leq \alpha_{i_j}(\mathbf{u}) \leq 1$, where α_{i_j} are so called shape functions determined by the ratio of areas [17], [18]. For example, α_{i_1} is equal to the ratio of the area of triangle pjj' to that of the total area A_i, shown in Fig. 1(a).

Within triangle T_i, the discrete energy $E_{T_i}(\phi(\cdot))$ becomes

$$\begin{aligned} &E_{T_i}(\phi(\cdot)) \\ &\doteq \frac{\int_{T_i}\|\nabla\phi_{T_i}(\mathbf{u})\|^2 d\mathcal{M}}{\int_{T_i}\phi_{T_i}(\mathbf{u})^2 d\mathcal{M}} \\ &= \frac{\sum_{j=1}^{3}\sum_{j'=1}^{3}\int_{T_i}\left\langle\nabla\alpha_{ij},\nabla\alpha_{ij'}\right\rangle\phi\left(\mathbf{u}_{ij}\right)\phi\left(\mathbf{u}_{ij'}\right)d\mathcal{M}}{\sum_{j=1}^{3}\sum_{j'=1}^{3}\int_{T_i}\alpha_{i_j}\alpha_{i_{j'}}\phi\left(\mathbf{u}_{i_j}\right)\phi\left(\mathbf{u}_{i_{j'}}\right)d\mathcal{M}}. \end{aligned}$$

Assume K_{T_i} and Q_{T_i} to be 3×3 matrices. The jj'th entry of K_{T_i} is $\int_{T_i}\alpha_{i_j}\alpha_{i_{j'}}d\mathcal{M}$, and the jj'th entry of Q_{T_i} is $\int_{T_i}\langle\nabla\alpha_{ij},\nabla\alpha_{ij'}\rangle d\mathcal{M}$ [17], [18]. Therefore, the energy within triangle T_i takes the matrix form

$$E_{T_i}(\phi(\cdot)) = \frac{\Phi_{T_i}^t Q_{T_i}\Phi_{T_i}}{\Phi_{T_i}^t K_{T_i}\Phi_{T_i}}$$

as shown in the equation at the bottom of the page. The total energy is then obtained by assembling all triangle elements

$$E(\phi(\cdot)) = \sum_{i=1}^{N_T} E_{T_i}(\phi(\cdot)) = \frac{\sum_{i=1}^{N_T}\Phi_{T_i}^t Q_{T_i}\Phi_{T_i}}{\sum_{i=1}^{N_T}\Phi_{T_i}^t K_{T_i}\Phi_{T_i}}. \quad (20)$$

Reorganize by Vertex Contribution and Rewrite as Matrix Form: Define $N_v \times N_v$ sparse matrices Q and K. As depicted in Fig. 1(b), the jth row of matrix Q corresponding to vertex j has diagonal entry $Q_{jj} = (1/2)\sum_{i\in N_T(j)}(\cot\theta_{i_{jj_1}} + \cot\theta_{i_{jj_2}})$ and off-diagonal entries $Q_{jj'} = -(1/2)(\sum_{i\in N_T(jj')}\cot\theta_{i_{jj'}})$; Q is a semi-positive definite matrix (see Appendix). Similarly, the jth row of matrix K has diagonal element $K_{jj} = (1/6)\sum_{i\in N_T(j)}A_i$ and off-diagonal entries $K_{jj'} = (1/12)\sum_{i\in N_T(jj')}A_i$; K is a positive definite matrix since it is strictly diagonally dominant and diagonal entries are positive. The total energy has the matrix form

$$E(\Phi) = \frac{\Phi^t Q\Phi}{\Phi^t K\Phi}. \quad (21)$$

Seek CON Basis of Eigen-Elements: The orthonormal basis functions (Φ) subject to normalization and boundary conditions are critical points of the weak form of the LB eigenvalue problem in (21) so that they satisfy the equation

$$Q\Phi = \lambda K\Phi \quad (22)$$

which is a generalized algebraic eigenvalue problem. Note, the trivial orthonormal basis function with zero eigenvalue is convened to be indexed by $i = 0$, $\phi_0(\mathbf{u}) = (1/\sqrt{\mathcal{M}})$ and $\lambda_0 = 0$.

2) Implementation: Implementation steps involved in computing LB orthonormal basis functions on the cortical manifold are summarized as follows:

- define region of interest in magnetic resonance imaging (MRI) volume;
- segment region of interest into white matter, gray matter, and CSF using Bayesian segmentation method;
- generate a triangulated mesh by matching tetrahedra;
- refine triangulation of the mesh using optimization procedure;
- extract subsurface delineated by dynamic programming on the cortical manifold;
- construct matrices Q and K for the submanifold;
- solve eigenfunctions and eigenvalues of problem (22) using generalized symmetric eigenvalue problem solver, named "sygvxeig," in LAPACK library [27].

$$\Phi_{T_i} = \begin{bmatrix}\phi(v_{i_1})\\ \phi(v_{i_2})\\ \phi(v_{i_3})\end{bmatrix}, \quad K_{T_i} = \frac{A_i}{12}\begin{bmatrix}2&1&1\\1&2&1\\1&1&2\end{bmatrix},$$

$$Q_{T_i} = \frac{1}{2}\begin{bmatrix}\cot\theta_{i_{12}}+\cot\theta_{i_{13}} & -\cot\theta_{i_{12}} & -\cot\theta_{i_{13}}\\ -\cot\theta_{i_{12}} & \cot\theta_{i_{12}}+\cot\theta_{i_{23}} & -\cot\theta_{i_{23}}\\ -\cot\theta_{i_{13}} & -\cot\theta_{i_{23}} & \cot\theta_{i_{13}}+\cot\theta_{i_{23}}\end{bmatrix}$$

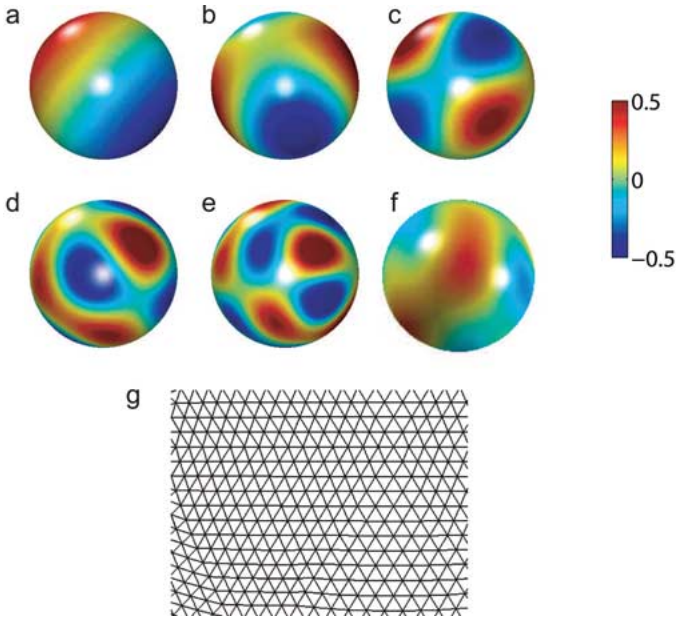

Fig. 2. Spherical harmonics. (a)–(e) show numerical solutions to the 2nd, 6th, 12th, 17th, and 28th harmonics on the unit sphere. A linear combination of these five harmonics constructs a function, $f = 0.2\phi_2 + 0.4\phi_6 + 0.2\phi_{12} + 0.2\phi_{17} + 0.2\phi_{28}$, shown in (f). (g) Part of the triangulation of this sphere is shown.

The convergence of the numerical solution for the eigenvalue problem (22) is dependent on the quality of the triangulated mesh but not on its topology. The ratio of the biggest triangle area to the smallest triangle area on the triangulated mesh and interior angles of each triangle determine the conditional number of matrices K and Q. Therefore, we refine the triangulated mesh to a more uniform graph by locally moving vertices to minimize energy based on the distance between vertices in Step 4 (see details of refining the triangulated surface in [28]). The purpose of this step is to guarantee to find numerical solutions of basis functions. The accuracy of the numerical solutions to the eigenvalue problem is determined by the refinement and quality of the triangulated surface.

D. Examples

We illustrate numerical solutions to LB orthonormal basis functions on a unit sphere and brain manifold.

The closed form of continuous spherical harmonics has been given in (1). Here, we illustrate their numerical solutions obtained using the algorithm in Section III-C. Empirically, a unit sphere is discretized into 20480 triangles with 10242 vertices [see Fig. 2(g)]. Fig. 2(a)–(e) shows the five harmonics: $\phi_2, \phi_6, \phi_{12}, \phi_{17}, \phi_{28}$. The region with positive values is colored by red, while the one with negative values is denoted by blue. As one goes to higher order of the spherical harmonics, the alternating red/blue pattern varies rapidly, implying the inclusion of high frequency components; this is similar to Fourier basis functions in one-dimensional case. Instead of estimating κ_{ls} in an inverse problem (4), we constructed a function f, $f = 0.2\phi_2 + 0.4\phi_6 + 0.2\phi_{12} + 0.2\phi_{17} + 0.2\phi_{28}$, shown in Fig. 2(f). Such a function f is a continuous and differentiable function on the sphere.

For a brain manifold, there are no closed-form expressions of the LB orthonormal basis functions. We give an example of numerical solutions to orthonormal basis functions on the planum temporale in Fig. 3. The planum temporale manifold is discretized into 2558 triangles with 1346 vertices [see Fig. 3(h)]. Fig. 3(a)–(f) shows basis functions $\phi_i, i = 2, 3, \ldots, 7$. A smooth function constructed by the average of these basis functions is given in Fig. 3(g).

IV. Spline Smoothing Problem

For the completeness, we recall the smoothing problem in (3) defined on the unit sphere in Section II and generalize it to an arbitrary 2-D manifold $\mathcal{M}$. The data model on the manifold associated with the smoothing problem is the same as (2) and rewritten as

$$y(\mathbf{u}) = f(\mathbf{u}) + \epsilon(\mathbf{u})$$

where $f(\mathbf{u})$ is a function defined on $\mathcal{M}$. $\epsilon(\mathbf{u})$ is independent and identically Gaussian distributed noise with zero mean and variance σ^2. A smooth representation of f is obtained by minimizing

$$f(\mathbf{u}) = \underset{f(\cdot)\in C^2(\mathcal{M})}{\arg\min}\ \gamma \int_{\mathcal{M}} \|\nabla f\|^2 d\mathcal{M} + \sum_{i=1}^{N} (y_i - f(\mathbf{u}_i))^2 \quad (23)$$

for some $\gamma > 0$. This expression represents a tradeoff between fidelity to the data, as represented by the residual sum of squares, and smoothness of the solution, as represented by the square integral of the first derivative. Instead of using the expansion of f over basis ϕ_i, $f(\mathbf{u}) = f_0 + \sum_{i=1}^{\infty} \kappa_i \phi_i(\mathbf{u})$, we give an equivalent form by following the Representer Theorem [29]. It states that the minimizer $f(\mathbf{u})$ of the variational problem (23) lies in a finite dimensional subspace and admits a representation in the form

$$f(\mathbf{u}) = f_0 + \sum_{k=1}^{N} \beta_k G(\mathbf{u}, \mathbf{u_k}) \quad (24)$$

where the LB kernel $G(\cdot,\cdot) : D \times D \mapsto \mathbb{R}, D \subset \mathbb{R}$ is a real-valued function given by

$$G(\mathbf{u_1}, \mathbf{u_2}) = \sum_{i=1}^{\infty} \frac{1}{\lambda_i} \phi_i(\mathbf{u_1}) \phi_i(\mathbf{u_2}). \quad (25)$$

ϕ_i and λ_i are orthonormal basis functions and eigenvalues of the LB operator. Since the LB is a self-adjoint operator, the infinite series on the right-hand converges for any $\mathbf{u_1}$ and $\mathbf{u_2}$ and kernel $G(\mathbf{u_1}, \mathbf{u_2})$ is positive definite. Therefore, $G(\mathbf{u_1}, \mathbf{u_2})$ defines r.k.h.s [15] with the reproducing property of $G(\mathbf{u_1}, \mathbf{u_2})$: for any function $f \in C^1(\mathcal{M})$ which satisfies Neumann boundary conditions in (17), we have

$$\int_{\mathcal{M}} \langle \nabla f(\cdot), \nabla G(\cdot, \mathbf{u}) \rangle \, d\mathcal{M} = f(\mathbf{u}). \quad (26)$$

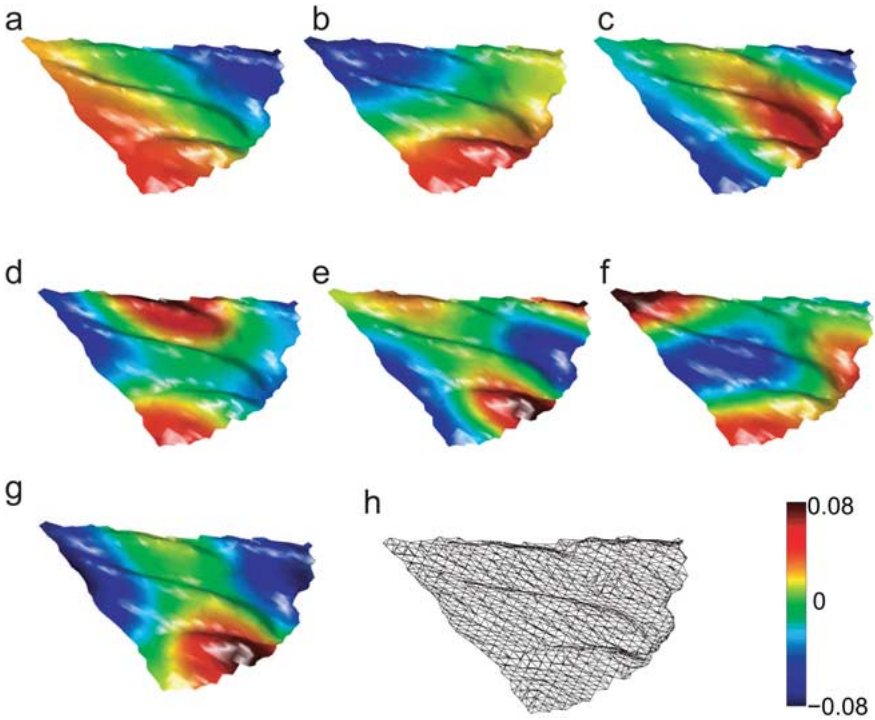

Fig. 3. (a)–(f) Six orthonormal basis functions, ϕ_i, $i = 2, \ldots, 7$, of the LB operator associated with the manifold of planum temporale are shown. (g) Gives a function (f) constructed by a linear combination of these six basis functions $f = (1/6)\sum_{i=2}^{7}\phi_i$. (h) Illustrates the triangluated mesh of this manifold.

It can be proven that both expressions of the expansion of f over basis ϕ_i and (24) are the representations of the minimizer of the variational problem in (23). The relationship between κ_i and β_k are

$$\kappa_i = \frac{1}{\lambda_i}\sum_{k=1}^{N}\beta_k\phi_i(\mathbf{u}_k), \quad i = 1, 2, \ldots, \infty$$

$$\beta_k = y_k - f_0 - \sum_{i=1}^{\infty}\kappa_i\phi_i(\mathbf{u}_k), \quad k = 1, 2, \ldots, N.$$

To find the solution to the smoothing problem, (24) shows that the minimizer of (23) is completely determined by the scalar f_0 and N-dimensional vector $\beta = (\beta_1, \beta_2, \cdots, \beta_N)^t$. Consequently, the variational functional on the right-hand side of (23) can be treated as a function of f_0 and β. By the reproducing property of $G(\mathbf{u_1}, \mathbf{u_2})$, the variational problem (23) is equivalent to the following quadratic minimization problem:

$$\{\hat{f}_0, \hat{\boldsymbol{\beta}}\} = \underset{f_0\in\mathbb{R}, \boldsymbol{\beta}\in\mathbb{R}^N}{\arg\min}\ \gamma\boldsymbol{\beta}^t G\boldsymbol{\beta} + ||G\boldsymbol{\beta} + f_0\mathbf{e} - \mathbf{y}||^2 \qquad (27)$$

where G is a $N \times N$ matrix with $G(\mathbf{u}_i, \mathbf{u}_j) = \sum_{k=1}^{M}(1/\lambda_k)\phi_k(\mathbf{u}_i)\phi_k(\mathbf{u}_j)$ as the ijth entry and $\mathbf{e}$ is a vector with one as entry. The solution $\hat{f}_0, \hat{\boldsymbol{\beta}}$ of the minimization problem (27) satisfies the following linear system:

$$(G + \gamma I)\hat{\boldsymbol{\beta}} + \hat{f}_0\mathbf{e} = \mathbf{y} \qquad (28)$$

$$\langle \mathbf{e}, \hat{\boldsymbol{\beta}}\rangle = 0. \qquad (29)$$

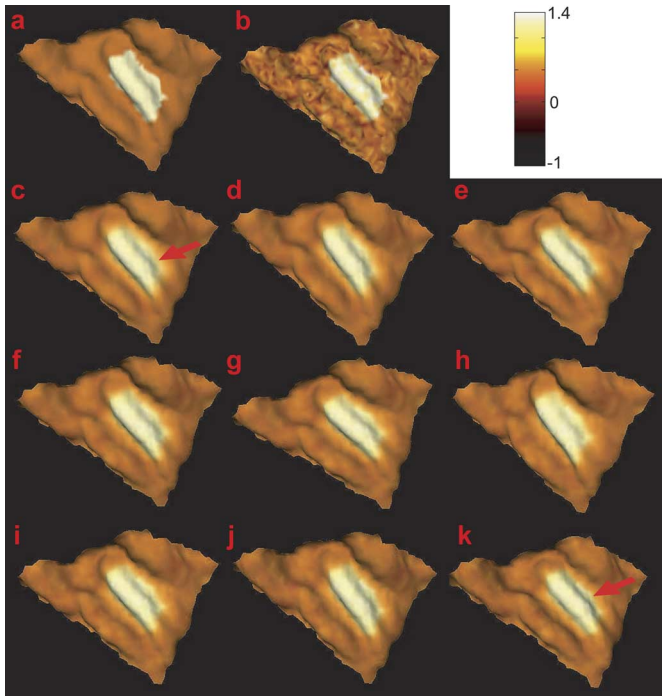

Fig. 4. Synthetic data. (a) Illustrates the ground truth f on the manifold of the planum temporale shown in Fig. 3. f is defined in such a way that the value of f on the small region inside the manifold is 1.0, otherwise 0. (b) Shows the function contaminated by a Gaussian noise with zero mean and standard deviation 0.2. (c)–(k) Show its smoothed functions by 10%, 20%, $\cdots$, 90% of orthonormal basis functions out of 1346 basis functions. Red arrows point out where there are slight differences.

V. Results

In this section, a synthetic example is given to intuitively illustrate the performance of the smoothing method and how many basis functions should be incorporated into the kernel (25). Then, we show three applications in MRI studies: smoothing mean curvature, cortical thickness, and functional

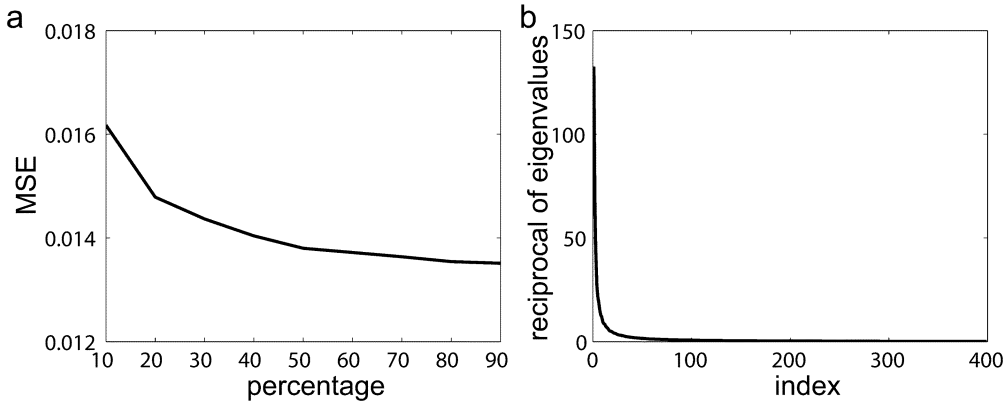

Fig. 5. (a) Illustrates a plot of MSE between the smoothed functions and the ground true versus the percentage of orthonormal basis functions used in the smoothing for Fig. 4(c)–(k). (b) Shows multiplicative inverses of the first four hundred eigenvalues of the manifold in Fig. 4(a).

statistical maps on brain manifolds (cingulate, planum temporale, and occipital lobe).

A. Quantitative Evaluation

For the demonstration of the performance for the smoothing method, we generated a function f on the planum temporale manifold in such a way that f is equal to 1.0 in the piece of interior region [see Fig. 4(a)], otherwise 0. The Gaussian noise with zero mean and standard deviation 0.2 was added into f everywhere on the manifold shown in Fig. 4(b). The 10%, 20%, $\cdots$, 90% of total number of basis functions were used to construct the kernel in (25). The smoothed results are sequentially shown in Fig. 4(c)–(k). There is no significant difference among these results, except the boundary pointed out by red arrows becomes sharper as more basis functions are incorporated. In Fig. 5(a), the MSE between these results and the ground truth in Fig. 4(a) is plotted as a function of percentage of basis functions having been used. The small change in MSE also implies such subtle difference among these smoothed results. The reason we see this is due to the fact that reciprocals of the LB eigenvalues, $(1/\lambda_i)$, on planum temporale rapidly decreases so that high order basis functions give a small amount of contribution in the kernel (25), shown in Fig. 5(b), which implies that small number of the basis functions are needed in the smoothing and can be determined by the distribution of eigenvalues. As for this manifold, 256 out of total 1346 orthonormal basis functions contribute 90% of total energy, $\sum_{i=2}^{256}(1/\lambda_i) \approx 0.9 \sum_{i=2}^{1346}(1/\lambda_i)$.

B. Mean Curvature Maps

The human brain is highly curved structure with gyri and deep sulci, which can be identified by the curvature information. However, the curvature information has high order differential nature, initial estimates from methods in [30] and [31] are sensitive to noise. Therefore, smoothing curvature maps becomes a crucial step in many applications to guarantee finding true solutions. For example, gyrus crown or sulcus valley can be delineated via dynamic programming optimization using curvature information [26]. Moreover, the folding pattern was studied using the scale-space primal sketch of the cortex mean curvature [3].

Fig. 6 shows mean curvature maps on cingulate manifolds where have been reported to be the brain region relative to neuropsychiatric diseases with emotional, motivation, attention symptoms, such as Schizophrenia and Alzheimer's disease (e.g., [32]). Fig. 6(a) and (b) illustrate original mean curvature maps on left and right cingulate manifolds discretized into 30583 and 30847 triangles with 15746 and 15861 vertices, respectively. Dark color corresponds to the sulcus with negative mean curvature, while the bright color denotes the gyrus with positive mean curvature. The bottom row illustrates smoothed versions of mean curvature maps.

C. Cortical Thickness Maps

The cortical thickness extracted directly from MRI is a very important measurement in a wide variety of studies on neurodegenerative and psychiatric disorders by many groups [5], [32]–[42]. Noisy cortical thickness maps on the cortical manifold may cause spurious results in a large population study. Properly smoothing cortical thickness maps on the cortical manifold not only increases signal to noise ratio but also makes the thickness data suitable for parametric statistical models (e.g., [5]).

Fig. 7 shows cortical thickness maps on left and right planum temporale (PT), the region implicated in a variety of neuropsychiatric and neurodevelopmental disorders, (e.g., schizophrenia, bipolar, auditory disorders [26], [43]–[45]). We delineate the boundary of PT cortical manifolds by tracking principal curves from the retro-insular end of the Heschl's Gyrus (HG) to the superior temporal gyrus (STG), along the posterior STG up to the start of the ramus and back to the retro-insular end of the HG via dynamic programming [26]. The thicker region is colored brightly, while the dark color denotes the thinner region. The top row shows left and right PT manifolds colored by the cortical thickness information. The manifolds are represented by 2891 and 2636 triangles with 1519 and 1408 vertices from the left to the right column, respectively. The smoothed cortical thickness maps are depicted in Fig. 7(c) and (d).

D. Functional Statistics Smoothing

Such an approach can be used for structural as well as functional maps. Fig. 8(a) shows the functional activation of the

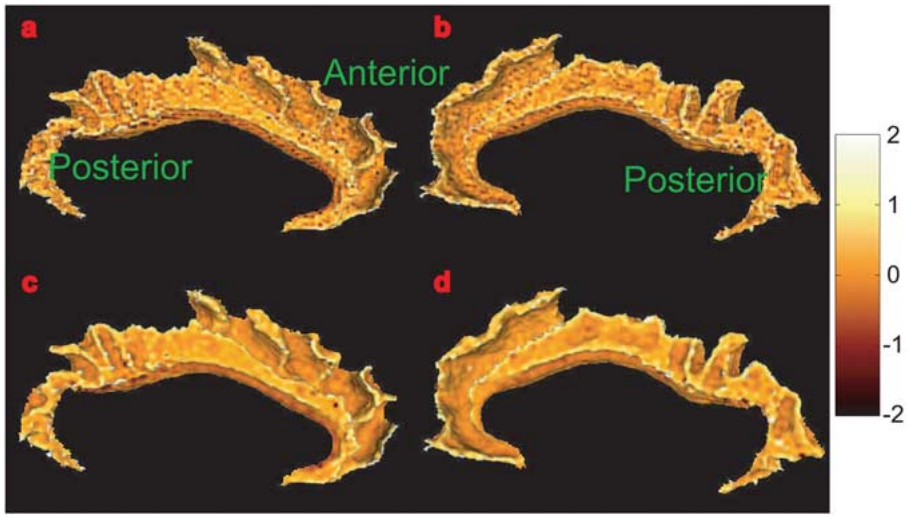

Fig. 6. Mean curvature maps of cingulate manifolds. (a) and (b) Show original mean curvature maps on the left and right cingulate. (c) and (d) Give their smoothed curvature maps. Each manifold is represented by 30583 and 30847 triangles with 15746 and 15861 vertices from the left to the right column.

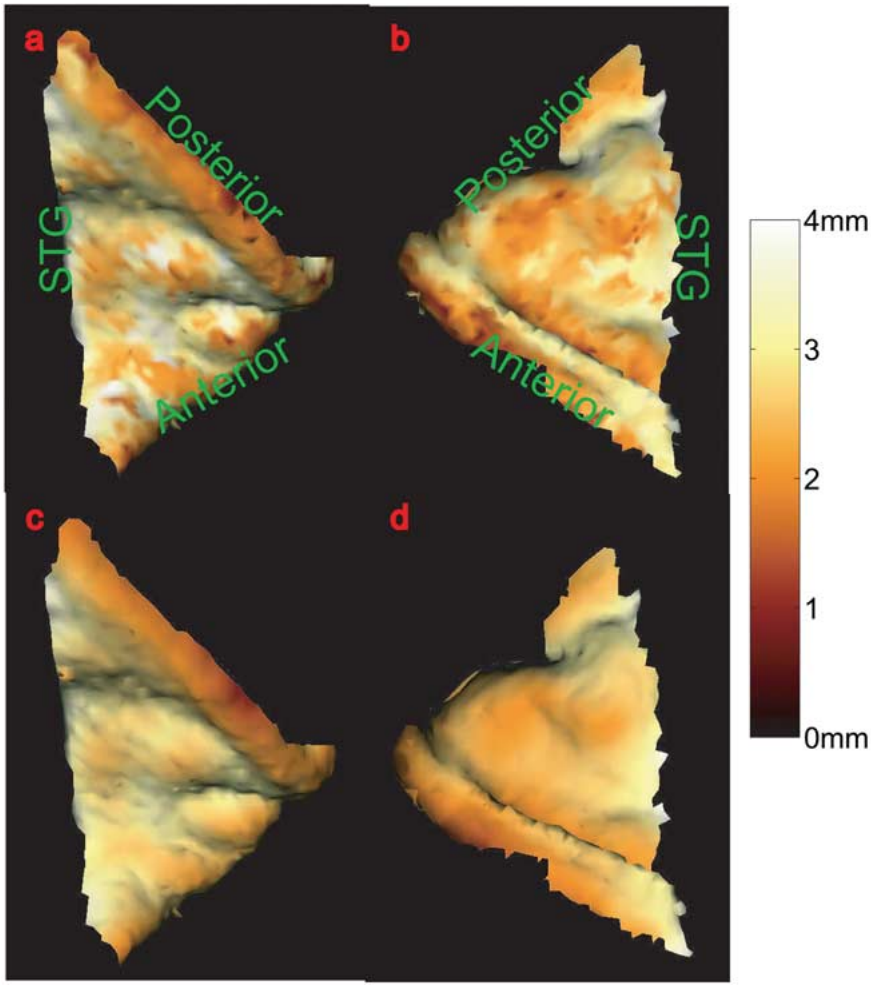

Fig. 7. Cortical thickness maps visualized on the manifolds of planum temporale. (a) and (b) Show original cortical thickness maps on the left and right planum temporale, which are discretized into 2891 and 2636 triangles with 1519 and 1408 vertices, respectively. (c) and (d) Illustrate their smoothed maps. "STG" denotes the superior temporal gyrus. Anterior boundary is defined at the location of posterior Heschl's sulcus and the posterior boundary is delineated by the curve started from the ramus and back to the restro-insular end of the HG.

stationary ring stimuli on the right occipital lobe manifold to study the retinotopic maps in the visual cortex [46]. Stimuli are stationary rings defined as 1, 2, 3, 4, 5 from the smallest size (inner radius: 1.5°) to the largest size (outer radius: 12.8°) and

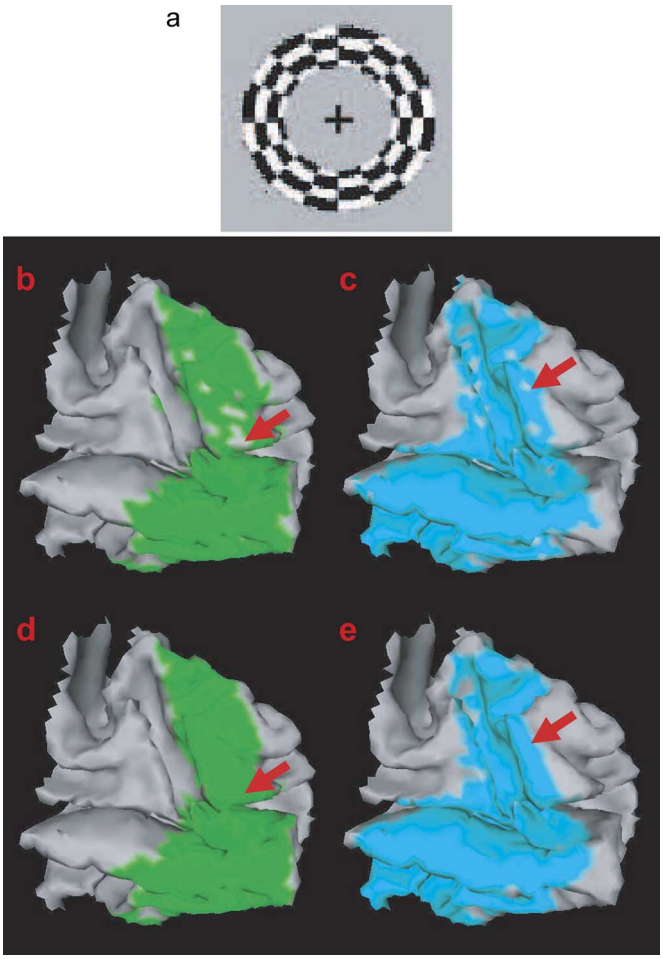

Fig. 8. Functional activation on the right occipital lobe manifold. (a) Shows the stationary ring stimulus; a cross is placed at cortical locations responding preferentially to near-fovea. (b) and (d) Show original and smoothed functional response to stationary ring stimulus with inner radius as 3.5° and outer radius as 5.4° on the right occipital manifold. Similarly, the right column [(c) and (e)] show the original and smoothed response maps to the ring with inner radius as 5.4° and outer radius as 8.3°. Red arrows point out where the holes on the original functional maps are closed on the smoothed maps.

central disk defined as d (radius: 1.5°). During a 72-s cycle, six stimuli are shown on the screen for 12 s in the order 5, 3, 1, 4, 2, and d; four cycles are in each run. By using the general linear regression model, we compute the t-statistics for each ring's response versus others in the functional magnetic resonance imaging (fMRI) volume, and then superimpose the positive t-value on the occipital manifold. The t-statistics map is smoothed on the manifold represented by 11512 triangles with 5896 vertices. Finally, the significant retinotopic activation is shown by giving the threshold. Fig. 8(b) depicts the retinotopic activations to ring 3 (inner radius as 3.5° and outer radius as 5.4°) on the manifold. Fig. 8(d) depicts the response to ring 4 (inner radius as 5.4° and outer radius as 8.3°) on the manifold. Smoothed results associated with them are shown in Fig. 8(d) and (e), respectively. Red arrows emphasize the place where the holes on the original functional response maps are closed on the smoothed maps.

VI. Conclusion

In this paper, we have generalized the spline smoothing problem from a unit sphere to an arbitrary Riemannian manifold with boundaries. The paper has focused on the use of the LB operator for the generation of a complete set of real-valued orthonormal basis functions on the manifold embedded in $\mathbb{R}^3$. Neumann boundary conditions taken into account are suitable to smooth surface metrics on an open manifold of the brain. The power of the approach taken is that such a basis for each curved cortical manifold is an ideally suited basis for representing and smoothing functions such as curvature, thickness, and functional responses intrinsically to the local coordinates of the individual neocortex. Furthermore, this approach generalizes the Fourier orthonormal representation of functions on the Euclidean regular grid to the orthonormal representation of functions on an arbitrary manifold. The stochastic signal processing procedure can be simply applied on the manifold.

The proposed method from classical FEM is a robust approach for computationally generating base. FEM for solving the diffusion equation on brain manifolds can also be found in references [7], [9]. This method is robust in a sense that it discretizes the LB operator in the volume rather than on the manifolds themselves. Compared to finite difference method, the boundary of manifolds can be taken into account automatically without expanding the region. For example, applying the Laplace operator on a regular Euclidean square, we used to expand the square to give a boundary information so that the solution is equivalent to what is obtained by finite element method. However, it is difficult to expand local coordinates on manifolds to have the same formulation as on the Euclidean coordinate system.

Such an approach recovers continuous functions on the brain manifolds, which is a crucial step in many brain image applications. For instance, the smoothed representation of the curvature map is helpful to accurately delineate gyri or sulci on brain manifold [3], [26]. For functional statistical maps, this approach clusters activation based on the statistics of the neighborhood, which implies that the activation at one vertex on the manifold is significant but it may not be shown after smoothing due to the weak activation of the vertex's neighbors.

Specific work on the application of the diffusion equation with the LB operator for smoothing and interpolation can as well be found in [4], [5], [7]–[11] and [47]. The diffusion smoothing is an iterative process and stop criterion is hard to control. In this paper, our smoothing problem is an algebraic problem and directly gives the solution for a data model with Gaussian noise, $y(u) = f(u) + \epsilon(u)$. Moreover, in the practical point of view, basis functions can be used to smooth different functions on a manifold, (e.g., curvature maps, functional maps, and cortical thickness maps). In addition, our approach taken here is a significant extension of these diffusion equation smoothing methods to the induction of Gaussian random field models on the neocortex for studying intrinsic properties of the cortex. In details, such a Gaussian random field $\{f(\mathbf{u}) = \sum_{i=1}^{\infty} f_i \phi_i(\mathbf{u})\}$, where $\{f_i, i = 1, \cdots, \}$ are independent, Gaussian random variables with fixed means $E\{f_i\} = \mu_i$ and variances $E\{f_i^2\} - E^2\{f_i\} = \sigma_i^2$. The Gaussian field is completely specified by

its mean and covariance operator, $E\{f\} = \sum_{i=1}^{\infty} \mu_i \phi_i, K_f = \sum_{i=1}^{\infty} \sigma_i^2 \phi_i \phi_i^t$. Then, a statistical testing (e.g., Hotelling T^2 test) can be directly applied to such a coefficient vector f_i instead of $f(\mathbf{u})$. This framework is very useful to investigate differences in cortical thickness and functional statistical maps on the cortex as well as cortical shape analysis. Such a framework extends the previous work on surface harmonic representation for shapes such as curved manifolds. The earliest work in computer vision was that of Pentland and Sclaroff on surface harmonics in the deterministic setting [48]. Joshi [28] then extended this for stochastic representations such as appropriate for morphometric inference such as being pursued by the Csernansky group in the hippocampus [2], [49].

APPENDIX

Week Form of the Eigenvalue Problem

The eigenvalue problem in (15) for the LB operator is equivalent to the variational problem in (19), where eigenfunctions are subject to Neumann boundary conditions given in (17).

Proof: From the divergence theorem, for a real-valued function $\nu(\mathbf{u})$ in $C^2(\mathcal{M})$, we have

$$\int_{\mathcal{M}} \left(-\Delta\phi(\mathbf{u})\right) \nu(\mathbf{u}) d\mathcal{M} = \int_{\mathcal{M}} \langle \bigtriangledown \phi(\mathbf{u}), \bigtriangledown \nu(\mathbf{u}) \rangle \, d\mathcal{M} + \int_{\partial \mathcal{M}} \nu(\mathbf{u}) \langle \nabla \phi(\mathbf{u}), \mathbf{n} \rangle \, dl. \quad (30)$$

Substituting Neumann boundary conditions yields

$$\int_{\mathcal{M}} - \left(\Delta\phi(\mathbf{u})\right) \nu(\mathbf{u}) d\mathcal{M} = \int_{\mathcal{M}} \langle \bigtriangledown \phi(\mathbf{u}), \bigtriangledown \nu(\mathbf{u}) \rangle \, d\mathcal{M}. \quad (31)$$

Replacing $\nu(\mathbf{u}) = \phi(\mathbf{u})$, we have

$$\int_{\mathcal{M}} - \left(\Delta\phi(\mathbf{u})\right) \phi(\mathbf{u}) d\mathcal{M} = \int_{\mathcal{M}} \|\nabla \phi(\mathbf{u})\|^2 \, d\mathcal{M}.$$

By multiplying (15) by ϕ and integrating, we see immediately that if ϕ satisfies (15), then

$$\int_{\mathcal{M}} \|\nabla \phi(\mathbf{u})\|^2 \, d\mathcal{M} = \lambda \int_{\mathcal{M}} |\phi(\mathbf{u})|^2 \, d\mathcal{M}$$

which tells λ satisfies (18).

If (18) is satisfied we have

$$[\lambda] \int_{\mathcal{M}} |\phi(\mathbf{u})|^2 \, d\mathcal{M} = \int_{\mathcal{M}} \|\nabla \phi(\mathbf{u})\|^2 \, d\mathcal{M}$$

and taking the gradient of the function $\lambda(\phi(\mathbf{u}) + \epsilon\nu(\mathbf{u}))$ with respect to ϵ and evaluating it at $\epsilon = 0$ we find

$$\delta[\lambda] \int_{\mathcal{M}} |\phi(\mathbf{u})|^2 \, d\mathcal{M} + 2[\lambda] \int_{\mathcal{M}} \nu(\mathbf{u}) \phi(\mathbf{u}) d\mathcal{M} = 2 \int_{\mathcal{M}} \langle \nabla \phi(\mathbf{u}), \nabla \nu(\mathbf{u}) \rangle \, d\mathcal{M}.$$

If $\delta[\lambda] = 0$, substituting (31) yields

$$\int_{\mathcal{M}} \left(-\Delta\phi(\mathbf{u}) - \lambda\phi(\mathbf{u})\right) \nu(\mathbf{u}) d\mathcal{M} = 0$$

for any $\nu(\mathbf{u})$. Therefore, we have

$$\Delta\phi(\mathbf{u}) + \lambda\phi(\mathbf{u}) = 0.$$

Q is Semi-Positive Definite

Matrix Q has the property that sum of each row and sum of each column are zero. It is obvious that Q has zero as an eigenvalue and an eigenvector with ones for all entries. In the following, we show that Q is a semi-positive definite matrix. To begin with proving that matrix Q_{T_i} in triangle T_i (see the right panel in Fig. 1) is semi-positive definite by showing that the determinants associated with all upper-left submatrices are nonnegative

$$\begin{aligned} &det\left|\cot\theta_{i_{12}} + \cot\theta_{i_{13}}\right| = \cot\theta_{i_{12}} + \cot\theta_{i_{13}} > 0 \\ &det\begin{vmatrix} \cot\theta_{i_{12}} + \cot\theta_{i_{13}} & -\cot\theta_{i_{12}} \\ -\cot\theta_{i_{12}} & \cot\theta_{i_{12}} + \cot\theta_{i_{23}} \end{vmatrix} = 1 \\ &det\left(Q_{T_i}\right) = 0. \end{aligned}$$

Assume B_i is a $N_v \times N_v$ matrix with upper-left submatrix Q_{T_i} and zeros for other entries. U_i is an identity matrix by swapping the first row with the jth row, the second row with the j_1th row, and the third row with the j_2th row. Matrix $U_i B_i U_i$ is also semi-positive definite. Matrix Q can be described by the sum of semi-positive definite matrices as the form

$$Q = \sum_{i=1}^{N_T} U_i B_i U_i.$$

If two matrices are semi-positive definite, then their sum matrix is semi-positive definite. So Q is a semi-positive definite matrix.

ACKNOWLEDGMENT

The authors thank Dr. P. Barta and Dr. S. Yantis of The Johns Hopkins University for providing planum temporale and fMRI data, and Dr. J. Csernansky of Washington University in St. Louis for providing cingulate data. They would also like to thank C. Poynton, A. Greenberg, and B. Rosenau for data analysis.

REFERENCES

[1] P. M. Thompson, K. M. Hayashia, E. R. Sowella, N. Gogtayb, J. N. Gieddb, J. L. Rapoportb, G. I. de Zubicarayc, A. L. Jankec, S. E. Rosec, J. Sempled, D. M. Doddrellc, Y. Wange, T. G. van Erpf, T. D. Cannonf, and A. W. Toga, "Mapping cortical change in Alzheimer's disease, brain development, and schizophrenia," *NeuroImage*, vol. 23, pp. S2–S18, 2004.

[2] J. G. Csernansky, L. Wang, S. C. Joshi, J. T. Ratnanather, and M. I. Miller, "Computational anatomy and neuropsychiatric disease: probabilistic assessment of variation and statistical inference of group difference, hemispheric asymmetry, and time-dependent change," *NeuroImage*, pp. S139–S150, 2004.

[3] A. Cachia, J.-F. Mangin, D. Rivière, F. Kherif, N. Boddaert, A. Andrade, D. Papadopoulos-Orfanos, J.-B. Poline, I. Bloch, M. Zilbovicius, P. Sonigo, F. Brunelle, and J. Régis, "A primal sketch of the cortex mean curvature: A morphogenesis based approach to study the variability of the folding patterns," *IEEE Trans. Med. Imag.*, vol. 22, no. 6, pp. 754–765, Jun. 2003.

[4] A. Andrade, F. Kherif, J. Mangin, K. J. Worsley, A. Paradis, O. Simon, S. Dehaene, D. Le Bihan, and J.-B. Poline, "Detection of fMRI activation using cortical surface mapping," *Hum. Brain Mapp.*, vol. 12, pp. 79–93, 2001.

[5] M. K. Chung, S. M. Robbins, K. M. Dalton, R. J. Davidson, A. L. Alexander, and A. C. Evans, "Cortical thickness analysis in autism with heat kernel smoothing," *NeuroImage*, vol. 25, pp. 1256–1265, 2005.

[6] P. Perona and J. Malik, "Scale-space and edge detection using anisotropic diffusion," *IEEE Trans. Pattern Anal. Mach. Intell.*, vol. 12, no. 7, pp. 629–639, Jul. 1990.

[7] M. K. Chung, K. J. Worsley, and A. C. Evans, "Tensor-based brain surface modeling and analysis," in *Proc. IEEE Comput. Soc. Conf. Comput. Vision Pattern Recognit.*, 2003, vol. 1, pp. I-467–I-473.

[8] M. K. Chung, K. J. Worsley, S. Robbins, T. Paus, J. Taylor, J. Griedd, J. L. Rapoport, and A. C. Evans, "Deformation-based surface morphometry applied to gray matter deformation," *NeuroImage*, vol. 18, pp. 193–213, 2003.

[9] M. K. Chung, "Statistical morphometry in neuroanatomy," Ph.D. dissertation, Department of Mathematics and Statistics, McGill Univ., Montreal, QC, Canada, May 2001.

[10] F. Memoli, G. Sapiro, and P. Thompson, "Implicit brain imaging," *NeuroImage*, vol. 23, pp. S179–S188, 2004.

[11] M. Bertalmio, L.-T. Cheng, S. Osher, and G. Sapiro, "Variational problems and partial differential equations on implicit surfaces," *J. Computational Phys.*, vol. 174, pp. 759–780, 2001.

[12] C. Bajaj and G. Xu, "Anisotropic diffusion of subdivision surfaces and functions on surfaces," *ACM Trans. Graphics*, vol. 22, pp. 4–32, 2003.

[13] G. Xu, "Discrete Laplace-Beltrami operators and their convergence," *Comput. Aided Geometric Design*, vol. 21, pp. 767–784, 2004.

[14] L. Lopez-Perez, R. Deriche, and N. Sochen, "The Beltrami flow over triangulated manifolds," in *Lecture Notes in Computer Science*. Berlin, Germany: Springer-Verlag, 2004, vol. 3117, pp. 135–144.

[15] G. Wahba, *Spline Models for Observational Data*. Philadelphia,, PA: SIAM, 1990, vol. 58, CBMS-NSF Regional Conference Series in Applied Mathematics.

[16] J. Buser, *Geometry and Spectra of Compact Riemann Surfaces*. Boston, MA: Birkhüser, 1992.

[17] M. N. O. Sadiku, *Numerical Techniques in Electromagnetics*. Boca Raton, FL: CRC, 1992, pp. 407–438.

[18] P. P. Silvester and R. L. Ferrari, *Finite Elements for Electrical Engineers*. Cambridge, U.K.: Cambridge Univ. Press, 1983, pp. 1–32.

[19] M. P. D. Carmo, *Differential Geometry of Curves and Surfaces*. London, U.K.: Prentice-Hall, 1976.

[20] W. M. Boothby, *An Introduction to Differentiable Manifolds and Riemannian Geometry*. New York: Academic, 1986.

[21] A. Grigoryan, "Analytic and geometric background of recurrence and non-explosion of the brownian motion on Riemannian manifolds," *Bull. Amer. Math. Soc.*, vol. 36, pp. 135–249, 1999.

[22] L. Cairo and T. Kahan, *Variational Technique in Electromagnetics*. New York: Gordon and Beach, 1965.

[23] M. Joshi, J. Cui, K. Doolittle, S. Joshi, D. Van Essen, L. Wang, and M. I. Miller, "Brain segmentation and the generation of cortical surfaces," *NeuroImage*, vol. 9, pp. 461–476, 1999.

[24] M. I. Miller, A. B. Massie, J. T. Ratnanather, K. N. Botteron, and J. G. Csernansky, "Bayesian construction of geometrically based cortical thickness metrics," *NeuroImage*, vol. 12, pp. 676–687, 2000.

[25] N. Khaneja, M. I. Miller, and U. Grenander, "Dynamic programming generation of curves on brain surfaces," *IEEE Trans. Pattern Anal. Mach. Intell.*, vol. 20, no. 11, pp. 1260–1265, Nov. 1998.

[26] J. T. Ratnanather, P. E. Barta, H. N. A. Lee, N. Lee, N. G. Morris, A. C. Dziorny, M. K. Hurdal, G. D. Pearlson, and M. I. Miller, "Dynamic programming generation of boundaries of local coordinatized submanifolds in the neocortex: Application to the planum temporale," *NeuroImage*, vol. 20, no. 1, pp. 359–377, 2003.

[27] L. S. Blackford, J. Dongarra, J. D. Croz, S. Hammarling, M. Marinova, J. Wasniewsk, and P. Yalamov, *LAPACK95 Users' Guide*, V. A. Barker, Ed., 1st ed. Philadelphia, PA: SIAM, 2001.

[28] S. Joshi, M. I. Miller, and U. Grenander, "On the geometry and shape of brain sub-manifolds," *Int. J. Pattern Recognit. Artif. Intell.*, vol. 11, no. 8, pp. 1317–1343, 1997.

[29] G. Kimeldorf and G. Wahba, "Some results on Tchebycheffian splaine functions," *J. Math. Anal. Appl.*, vol. 33, pp. 82–95, 1971.

[30] S. C. Joshi, J. Wang, M. I. Miller, D. C. VanEssen, and U. Grenander, "Differential geometry of the cortical surface," in *Vision Geometry IV*, R. A. Melter, A. Wu, F. Bookstein, and W. Green, Eds. Bellingham, WA: SPIE, 1995, vol. 2573, pp. 304–311.

[31] B. Hamann, "Curvature approximation for triangulated surfaces," *Computing Suppl.*, vol. 8, pp. 139–153, 1993.

[32] M. I. Miller, M. Hosakere, A. R. Barker, C. E. Priebe, N. Lee, J. T. Ratnanather, L. Wang, M. Gado, J. C. Morris, and J. G. Csernansky, "Labeled cortical mantle distance maps of the cingulate quantify differences between dementia of the Alzheimer type and healthy aging," *Proc. Nat. Acad. Sci*, vol. 100, pp. 15 172–15 177, 2003.

[33] J. R. Meyer, S. Roychowdhury, E. J. Russell, C. Callahan, D. Gitelman, and M. M. Mesulam, "Location of the central sulcus via cortical thickness of the precentral and postcentral gyri on MR," *Amer. J. Neuroradiol.*, vol. 17, pp. 1699–1706, 1996.

[34] M. S. Albert, "Cognitive and neurobiologic markers of early Alzheimer disease," *Proc. Nat. Acad. Sci.*, vol. 93, pp. 13 547–13 551, 1996.

[35] M. J. DeLeon, A. E. George, J. Golomb, C. Tarshish, A. Convit, and A. Kluger *et al.*, "Frequency of hippocampal formation atrophy in normal aging and Alzheimer's disease," *Neurobiol. Aging*, vol. 18, pp. 1–11, 1997.

[36] C. R. Jack, Jr., R. C. Petersen, Y. C. Xu, S. C. Waring, P. C. O'Brien, E. Tangalos, G. E. Smith, R. J. Ivnik, and E. Kokmen, "Medial temporal atrophy on MRI in normal aging and very mild Alzheimer's disease," *Neurology*, vol. 49, pp. 786–790, 1997.

[37] J. A. Kaye, T. Swihart, D. Howieson, A. Dame, M. M. Moore, T. Karnos, R. Camicioli, M. Ball, B. Oken, and G. Sexton, "Volume loss of the hippocampus and temporal lobe in healthy elderly persons destined to develop dementia," *Neurology*, vol. 48, pp. 1297–1304, 1997.

[38] J. P. Vonsattel and M. DiFiglia, "Huntington disease," *J. Neuropath. Exp. Neurol.*, vol. 57, pp. 369–384, 1998.

[39] R. B. Zipursky, E. K. Lambe, S. Kapur, and D. J. Mikulis, "Cerebral gray matter volume deficits in first episode psychosis," *Arch. Gen. Psych.*, vol. 55, pp. 540–546, 1998.

[40] J. C. Morris, "Is Alzheimer's disease inevitable with age?: Lessons from clinicopathologic studies of healthy aging and very mild Alzheimer's disease," *J. Clin. Invest.*, vol. 104, pp. 1171–1173, 1999.

[41] B. Fischl and A. M. Dale, "Measuring the thickness of the human cerebral cortex from magnetic resonance images," *Proc. Nat. Acad. Sci.*, vol. 97, no. 20, pp. 11 050–11 055, 2000.

[42] P. M. Thompson, M. S. Mega, R. P. Woods, C. I. Zoumalan, C. J. Lindshield, R. E. Blanton, J. Moussai, C. Holmes, J. L. Cummings, and A. W. Toga, "Cortical changes in Alzheimer's disease detected with a disease specific population-based brain atlas," *Cereb. Cortex*, vol. 11, pp. 1–16, 2001.

[43] E. E. Southard, "On topographical distribution of cortex regions and anomalies in dementia praecox, with some account of their functional significance," *Amer. J. Insanity*, vol. 71, pp. 603–671, 1915.

[44] K. L. Narr, P. M. Thompson, T. Sharma, J. Moussai, R. Blanton, B. Anvar, A. Edris, R. Krupp, J. Rayman, M. Khaledy, and A. W. Toga, "Three-dimensional mapping of temporo-limbic regions and the lateral ventricles in schizophrenia: Gender effects," *Biol. Psychiatry*, vol. 50, pp. 84–97, 2001.

[45] K. L. Narr, P. M. Thompson, T. Sharma, J. Moussai, C. Zoumalan, J. Rayman, and A. W. Toga, "Three-dimensional mapping of gyral shape and cortical surface asymmetries in schizophrenia: Gender effects," *Amer. J. Psych.*, vol. 158, pp. 244–255, 2001.

[46] J. Sunness, T. Liu, and S. Yantis, "Retinotopic mapping of the visual cortex using FMRI in a patient with central scotomas from atrophic macular degeneration," *Ophthalmology*, vol. 111, pp. 1595–1598, 2004.

[47] C. Ballester, M. Bertalmio, V. Caselles, G. Sapiro, and J. Verdera, "Filling-in by joint interpolation of vector fields and gray levels," *IEEE Trans. Image Process.*, vol. 10, no. 8, pp. 1200–1211, Aug. 2001.

[48] A. Pentland and S. Sclaroff, "Closed-form solutions for physically based shape modeling and recognition," *IEEE Trans. Pattern Anal. Mach. Intell.*, vol. 12, no. 7, pp. 715–729, Jul. 1991.

[49] J. G. Csernansky, S. Joshi, L. Wang, J. W. Hallerparallel, M. Gado, J. P. Miller, U. Grenander, and M. I. Miller, "Hippocampal morphometry in schizophrenia by high dimensional brain mapping," *Proc. Nat. Acad. Sci.*, vol. 95, pp. 11 406–11 411, 1998.